N. Damer, M. Gomez-Barrero, K. Raja, C. Rathgeb, A. Sequeira,
M. Todisco, and A. Uhl (Eds.): BIOSIG 2023,
Lecture Notes in Informatics (LNI), Gesellschaft für Informatik, Bonn 2023

A Wrist-worn Diffuse Optical Tomography Biometric System

Satya Sai Siva Rama Krishna Akula[1], Sumanth Dasari[1], Keerti Bajaj[1], Bhuvan Chennoju[1], Tejaswi Dhandu[1], Mostafizur Rahman[1], Reza Derakhshani[1]

Abstract: We present a Diffuse Optical Tomography (DOT)based biometric system that uses interior anatomical information for better privacy and security instead of external traits such as face or fingerprint. The DOT system has a wearable form factor covering the lower forearm and the wrist, where anatomical structures in the optical path of the DOT optodes capture the unique internal patterns used for biometrics. Our DOT scanner is low-cost, using COTS near-infrared LEDs and sensors. Our design also incorporates wrist vein imaging as a secondary modality to supplement the DOT. This paper details the design of the DOT system and the ensuing machine-learning pipeline. We demonstrate the utility of the DOT as a stand-alone biometric modality and the efficacy of its fusion with wrist vein patterns. Our early experimental findings show promising results, using a pilot dataset to achieve an area under the receiver operating characteristic curve (ROC AUC) of 0.999138 and an equal error rate (EER) of 1.27% for the DOT modality. The AUC and EER were 0.999655 and 0.48% for the wrist vein imaging modality only and 0.99989 and 0.21% for the fusion of both modalities.

Keywords: Biometric authentication, Vein imaging, Diffuse optical tomography (DoT), Performance evaluation

1 Introduction

Biometric traits such as fingerprints, iris patterns, voice, and facial features are among the most popular, each with its own pros and cons. Different biometric modalities have also been combined to enhance recognition accuracy and robustness and to deter presentation attacks, giving rise to multimodal biometric systems [USJ20, Ga06]. This paper proposes a new multi-modal wrist-worn biometric system using Diffuse Optical Tomography (DOT) as the primary and vascular imaging as the secondary modality. The combination provides a simple unitary user experience while leveraging the near-infrared imaging of the deep structural elements of the forearm using a novel application of DOT in biometrics. While DOT [BCH16] is a known method and has been widely applied in various medical applications, to the best of our knowledge, we are the first to apply it to the wrist and lower forearm for biometric identification [Di05]. The addition of vascular arcades as a supplementary modality and the blending of the two using machine-learning techniques are among the other highlights of this work. Vascular patterns have long been known to exhibit distinct characteristics, even among identical twins [Kr20]. The introduction of forearm/wrist DOT, besides providing a new and powerful source of entropy, significantly

[1] School of Science and Engineering, University of Missouri, Kansas City

boosts the security of the system. The combination of vascular and DOT imaging as an internal biometric source is inherently harder to attain surreptitiously and harder to tamper with. Unlike the ubiquitous face biometrics, altering or replicating such internal structures raises the bar for potential attackers [Du08] [TY13].

To summarize our unique contributions, we demonstrate the feasibility of forearm DOT as a biometric modality and show the utility of simultaneously adding captured vein patterns from the same area to the mix through a pilot study. We also present our scanner design innovations, employing a multi-path continuous-wave DOT scanning using a near-infrared (NIR) sensor-illuminator mesh made out of affordable commercial off-the-shelf (COTS) components. Data pre-processing, fusion, and machine learning analytics are also presented as a part of the pipeline. The resulting hardware-software POC is capable of real-time, end-to-end enrollment and matching, providing a new secure biometric identification solution [HB09]. The rest of this paper is organized as follows: section 2 details the hardware setup, section 3 presents the methodology for hardware usage, section 4 presents data collection and evaluation, and Sections 5 and 6 outline the conclusion and acknowledgments.

2 DOT Wristband Design

The optical system employed in the DOT wristband design consists of NIR LEDs as the illumination source[Ch04] and NIR detector/sensor arrays. The LEDs and sensors are arranged in blocks for uniformity, as depicted in Figure 1. The selection of the 870 nm wavelength was based on the absorption coefficients for both oxygenated and deoxygenated hemoglobin[Ch14][Hi02].

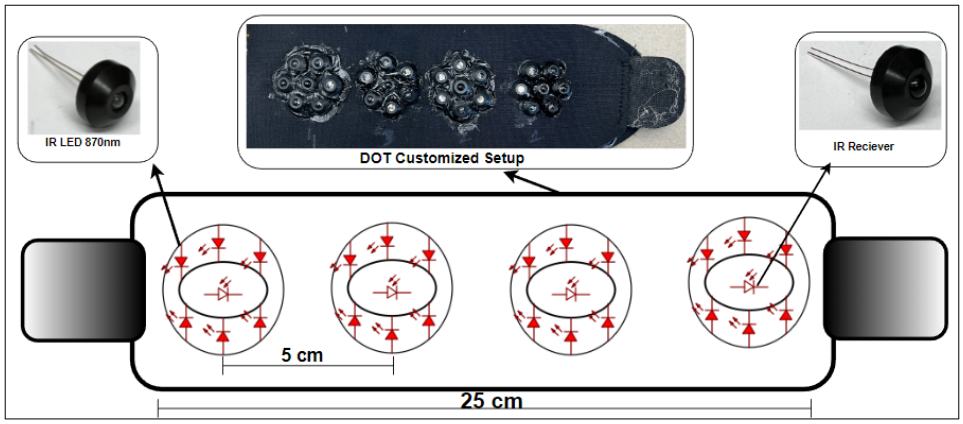

Fig. 1: DOT Wristband Setup

Several configurations of Infrared (IR) emitters and receivers were examined during the DOT design process. Experiments were conducted to explore distance ratios ranging from 1:1 to 1:6 between the IR receivers and emitters. Through these experiments, it was deduced that a 1:6 ratio with a 1.5cm gap between the components resulted in the best out-

comes. The final arrangement was determined to consist of one IR receiver and six IR emitters.

The setup shown in Figure 1 was finally selected. It consists of four units, namely S1, S2, S3, and S4. Each unit is comprised of a central IR sensor (100F5T-IR-JS-940NM) surrounded by six MTE8760N5 IR LEDs. The units were arranged linearly, with a 5 cm separation between the centers of adjacent units, as depicted in Figure 1. In the experimental setup, the control and communication of the sensors were facilitated by a Raspberry Pi (R Pi) device. The R Pi was the central controller and established a connection with an external host compute node. This arrangement enables the R Pi to exercise selective activation of pairs of blocks within the system.

In order to convert the analog signals received by the sensor into digital voltage values, an Adafruit ADS1115 Analog-to-Digital Converter (ADC) with a precision of 16 bits was employed. The utilized ADC can support sampling rates ranging from 8 to 860 samples per second and can be configured for 1 to 4 channels. It incorporates a programmable gain amplifier with a maximum gain of 16, which facilitates signal amplification. Communication with the ADC was established through I2C. The ADC can address up to 4 ADS1115 devices on a single 2-wire I2C bus, thereby allowing for a total of 16 single-ended inputs.

3 Methodology

This section describes the procedure for readings the DOT wristband signals. The DOT captures optical properties related to absorption and scattering, providing insights into tissue structure and function, with the former carrying the information of interest. The DOT method offers advantages in imaging deep tissue structures at shallow to medium depths. The positioning of Sensor-1 (S1), centrally on the palmar side of the hand near the nerve, with the wristband securely wrapped around the hand as shown in Figure 2(A), is the basis of the data collection apparatus. A 480-second data collection super-session was carried out, followed by the precise placement of the wristband 5 cm below the initial S1 location on the same hand to gather additional readings (in the future, the replication of the S1 optode array at multiple locations will obviate the need for this step). Given the proof of concept (POC) nature of this study[Yu05] [Hi02], the setup focuses on capturing data from two sensors (S1 and S2), despite the capability to capture data from four sensors. Consequently, two distinct files are obtained, with file-1 containing data from sensors S1 and S2 when the wristband is centered on the palmar side of the hand, and file-2 containing data from sensors S1 and S2 with the wristband positioned 5 cm below the previous hand location.

Our continuous-wave DOT specifically focuses on spatial patterns of absorption and scattering. The readings from the 16-bit ADC, Adafruit ADS1115, were converted to voltage values as follows:

$$Voltage = \frac{ADCReading * Full\ Scale\ Voltage}{(2^{16} * PGA)}$$

The frequency of anatomical DOT signals[HY16] are about zero given their permanence, however our sensors were capable of capturing higher-frequency biological signals [Xi19] [BS11], including heart rate (about 1 Hz), given that our ADC was operating at a sampling frequency of 128 Hz. The ADC device, configured with 2 channels and a programmable gain amplifier (PGA) setting of 2/3, facilitated the capture of signals within an absolute range of 0 to 43690. During the 480-second period ideally DOT should capture a total of

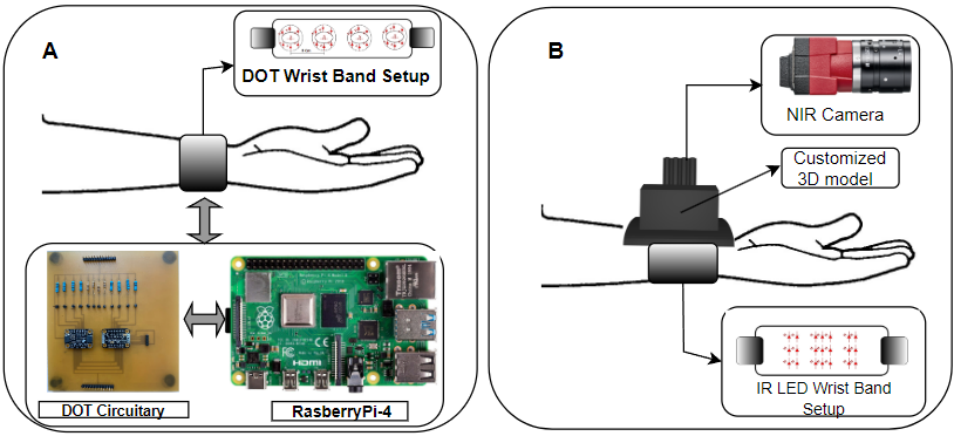

Fig. 2: (A) Setup to collect DOT signals and (B) Setup to collect IR vein images

30720 samples. However, factors such as the utilization of the Python spidev library and the limited processing speed of the Raspberry Pi as the master device introduced some overhead. As a result, approximately 25,000 readings, representing around 83.33 % of the original sensor data, were captured and saved. This data loss was considered negligible since the biological signals of interest (structural) exhibit significantly lower frequencies compared to the 128 Hz sampling rate. Section 4.2 details how this data was processed.

4 Data Collection and Evaluation

This section presents the methods used to evaluate the data collected with the experimental setup. The hardware captures DOT data and vein images. The data is then arranged as mated and unmated pairs and evaluated using a variety of metrics, including the false acceptance rate (FAR), the genuine acceptance rate (GAR), and the receiver operating characteristic (ROC) curve.

4.1 DOT and Vein Image Data Collection

This section shows samples of data that were collected. In Figure 3, images labeled A-1, A-2, A-3, and A-4, correspond to sensors S1, S2, S3, and S4, placed on different parts of the wrist. Images in 3A correspond to subject 1 and 3B correspond to subject 2. The placement

of the sensors is carefully considered to ensure accurate measurements, with Sensor S1 near the wrist providing potentially more precise readings than Sensor S4 positioned 5cm below the wrist on the dorsal side. Fig. 3 shows S1 - S4 readings for two subjects.

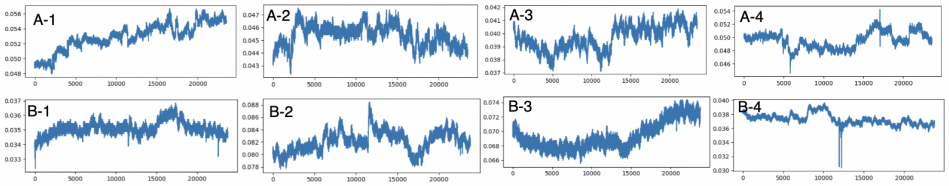

Fig. 3: DOT Readings A-x belongs to Subject 1, and B-x belongs to Subject 2, A-1, A-2, A-3, and A-4 belongs to sensors S1, S2, S3, and S4, respectively. S1 is placed on the palmar side near the wrist, S2 on the dorsal side near the wrist, S3 on the palmar side 5 cm below the wrist, and S4 on the dorsal side 5 cm below the wrist

The employed setup for IR imaging is depicted in Figure 2(B) and consists of a Customized IR camera hood and IR wristband. The IR Camera hood accommodates the NIR camera and is positioned 5 cm above the palmar side of the hand. The IR wristband comprises of three zones with a total of seven units interconnected in parallel, each unit containing 10 IR LEDs. These MTE8760N5 model IR LEDs operate at a wavelength of 870nm with a maximum power rating of 180mW. A regulated power supply maintains a consistent current of 50mA to the IR LEDs. When all three zones of the wristband are activated, IR light passes through the hand, making veins rich in deoxygenated hemoglobin visibly darker [Ji18] in the NIR image. The NIR camera used in this study is the Alvium 1800 U-501 NIR [Al], and the captured images are processed using the Vimba tool on a Windows PC. Adjustments to exposure and gain compensate for inter-subject variations and ensure consistent image quality, as shown in Figure 4. IR images labeled A and B demonstrate vein patterns under different configurations, including all LED zones, center zone only, sides only, and around the NIR camera.

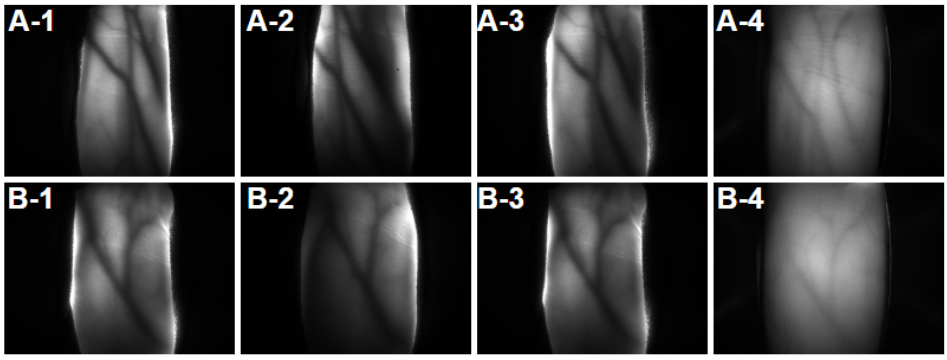

Fig. 4: IR images A-x belongs to Subject 1, and B-x belongs to subject 2, (A-1, B-1) - All LED zones on wristband turned on, (A-2, B-2) - Only Center zone LED's turned on, (A-3, B-3) Only LED's on either side turned on, (A-4, B-4) LED's around the NIR camera turned on.

4.2 Data Analysis

This section delves into the computations performed to process the raw data. The discussion covers data preprocessing, analysis, and interpretation, providing a comprehensive account of the computational procedures adopted.

Data Preprossessing: The data were acquired from 15 individuals with 9 trials per identity using the proposed DOT-vein scanner. The participants stayed still and breathed normally during the captures. Signals close to 1 Hz are primarily from the heartbeat. Thus Butterworth low pass filter with a 0.5Hz cut-off frequency was employed to filter out such non-structural DOT signals, followed by an outlier removal using the quantile techniques to ensure data quality. The DOT signal from each trial was segmented into multiple sub-signals and extracted the basic statistical features for each segment: the minimum, maximum, mean, and slope. This feature extraction reduced the time-dependent signals per channel to lower dimensions without losing the critical information that depends on the temporal signals. Table 1 shows the data preprocessing results. Feature extraction increased the feature space by approximately 12 folds, improving the subsequent comparisons and the machine learning algorithms.

	Raw Data			Processed Data		
Number of	Identities	Features	Trials	Identities	Features	Trials
	15	4	9	15	48	9

Tab. 1: Summary of Raw and Processed Data

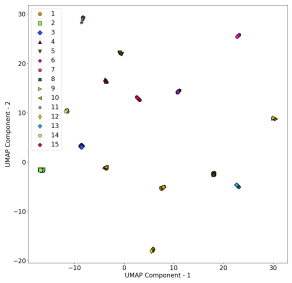

(a) UMAP for Visualizing DOT Data Separability

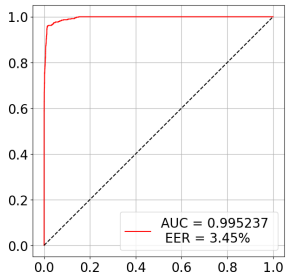

(b) ROC Curve for DOT Modality (all 9 trials)

Fig. 5: Visualizations of DOT data from 9 participants using tSNE and UMAP dimensionality reduction techniques.

Data Separability: The visualization in Figure 5a illustrates the application of visualization dimensionality reduction techniques on the feature-extracted DOT Data with 12 features per channel for all individuals and reveals partial clustering of identities in UMAP [MHM20] spaces. This confirms the separation of identities by the DOT signal, but some overlaps exist. Thus other approaches, such as distance-based matchers over various higher-dimensional feature spaces and other machine learning-based learners, were used to classify the DOT data better.

Similarity-based DOT Matching: This section presents the results of DOT verifications using cosine similarity as the similarity metric [Ib21] over 48 extracted features per identity. Figure 5b illustrates the Receiver Operating Characteristic (ROC) curve for 9 trials per individual, exhibiting an impressive AUC exceeding 0.99, indicating the accuracy of our DOT modality using a simple cosine similarity matcher, Whereas for the fusion 3 trials per each vein image were used to to be able to demonstrate the results with fusion.

4.3 Vein Image Matching

Datasets Used: As we mentioned earlier, our experimental hardware can also capture wrist vein patterns using incident and IR illumination. To create the vein matchers to go with the DOT, we utilized the publicly available finger vein dataset, the SCUT FV Presentation Attack Database (SCUT FVD) [Qi18]. Permission was obtained to use the dataset. The SCUT FVD dataset consists of vein images from 100 participants, with six fingers per individual and six vein images per finger, resulting in a total of 600 unique fingers and 3600 captures. By incorporating this dataset in our experiments, we aimed to evaluate the effectiveness of our proposed method in a challenging cross-dataset scenario.

Data Preprossessing and augmentation: The data pre-processing steps include random rotation up to 10 degrees), random horizontal flip, and color jittering. The latter involves making random modifications to the original image's brightness, contrast, saturation, and hue. This data augmentation step helps the model understand different representations of the data and increases the size of the pretraining dataset, enhancing the generalization capability of the model. A resizing step ensures that all input images have a uniform size of 224x224 pixels, matching the required input volume of our deep-learning models.

Deep Feature Extraction: We fine-tuned a ResNet50 pre-trained on ImageNet using the SCUTFVD dataset of finger vein images. We used the cross-entropy loss function for fine-tuning. Features are extracted from the 'flatten' layer of the model. We obtained features of 2048 dimensionality. Since the proposed experiment focuses on vascular veins, this model is fine-tuned further using the data captured with our experimental setup (See Section 3.). We captured the forearm and wrist area vein images for 15 subjects, 6 images from each, for 90 images. This dataset was further divided into the training set and test set with 3 images per subject in each subset, i.e., 50% split for train and test. Only a subject-dependent test has been demonstrated as the dataset collected is insufficient to demonstrate subject-independent results. The model discussed earlier was fine-tuned using the training subset data for 10 epochs. The features were then matched using cosine similarity; the ROC curve presents the verification performance over the test set.

4.4 DOT-Vein Fusion

The scores from the vein image features and the DOT data were averaged to obtain a single fusion score for each trial per individual. Fig 6c represents the ROC curve of this

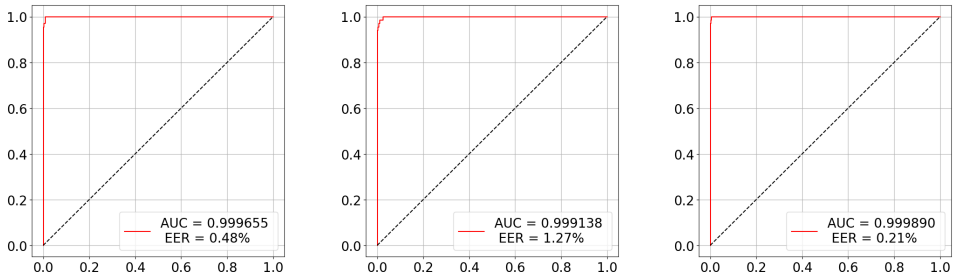

(a) Vein Image Modality (b) DOT Modality (3 trails only) (c) Fusion of both Modalities

Fig. 6: Receiver Operating Characteristic Curves for Biometric Data

fusion technique. Note that the results for vein image feature matching represent a subject-dependent protocol, where the identities (but not the images) used in training the models also appear for testing. But as the UTFVP dataset's experiment shows, with enough data, we can fine-tune the model to be able to extract quality features for subject-independent data as well.

5 Conclusion

Our pilot study shows that DOT of the forearm, as captured by our experimental wrist-worn scanner, has promise as a stand-alone biometric modality. We also showed that the secondary modality, wrist veins, can be fused with DOT to produce higher accuracy when compared to each modality by itself. The ROC AUC for the well-known vein image matching using deep features was 0.99965, yet a competitive 0. 99914 for the experimental DOT modality. The fusion of both modalities demonstrated an even better AUC of 0.99989. The vein image template matching technique exhibited a false acceptance rate of zero up to a genuine acceptance rate of 98.51%. Similarly, DOT data achieved a FAR of zero up to 74.81%. When both modalities were fused, the system achieved a zero FAR up to a GAR of 98.51%. This is a more desirable operating point, as operating at a low FAR is crucial for maintaining security and minimizing unauthorized access. We note that these results come from a very small pilot study, and thus a high observational variance must be considered. Our follow-up studies will be carried out using a larger data collection.

6 Acknowledgements

This work was sponsored by the Army Research Laboratory under Cooperative Agreement W911NF-21-2-0252. The views and conclusions contained are those of the authors and should not be interpreted as representing the official policies, either expressed or implied, of the Army Research Office or the U.S. Government. The U.S. Government is authorized to reproduce and distribute reprints for Government purposes, notwithstanding any copyright notation herein. Dr. Derakhshani is also a consultant for Jumio.

References

[Al] Alvium® 1800 USB Camera with High-Performance Sony Sensors: , Alvium 1800 U-501 NIR. Available online.

[BCH16] Barolet, Daniel; Christiaens, François; Hamblin, Michael R: Infrared and skin: Friend or foe. Journal of Photochemistry and Photobiology B: Biology, 155:78–85, 2016.

[BS11] Bagha, Sangeeta; Shaw, Laxmi: A real time analysis of PPG signal for measurement of SpO2 and pulse rate. International journal of computer applications, 36(11):45–50, 2011.

[Ch04] Christov, Ivaylo I: Real time electrocardiogram QRS detection using combined adaptive threshold. Biomedical engineering online, 3(1):1–9, 2004.

[Ch14] Chen, Chen; Tian, Fenghua; Liu, Hanli; Huang, Junzhou: Diffuse optical tomography enhanced by clustered sparsity for functional brain imaging. IEEE transactions on medical imaging, 33(12):2323–2331, 2014.

[Di05] Diamond, Solomon Gilbert; Huppert, Theodore J; Kolehmainen, Ville; Franceschini, Maria Angela; Kaipio, Jari P; Arridge, Simon R; Boas, David A: Physiological system identification with the Kalman filter in diffuse optical tomography. In: Medical Image Computing and Computer-Assisted Intervention–MICCAI 2005: 8th International Conference, Palm Springs, CA, USA, October 26-29, 2005, Proceedings, Part II 8. Springer, pp. 649–656, 2005.

[Du08] Ducros, Nicolas; da Silva, Anabela; Dinten, Jean-Marc; Peyrin, Francoise: Fluorescence diffuse optical tomography: A simulation-based study comparing time-resolved and continuous wave reconstructions performances. In: 2008 5th IEEE International Symposium on Biomedical Imaging: From Nano to Macro. pp. 388–391, 2008.

[Ga06] Galbally-Herrero, J; Fierrez-Aguilar, Julian; Rodriguez-Gonzalez, JD; Alonso-Fernandez, Fernando; Ortega-Garcia, Javier; Tapiador, Marino: On the vulnerability of fingerprint verification systems to fake fingerprints attacks. In: Proceedings 40th Annual 2006 International Carnahan Conference on Security Technology. IEEE, pp. 130–136, 2006.

[HB09] Hartung, Daniel; Busch, Christoph: Why vein recognition needs privacy protection. In: 2009 Fifth International Conference on Intelligent Information Hiding and Multimedia Signal Processing. IEEE, pp. 1090–1095, 2009.

[Hi02] Hielscher, AH; Bluestone, AY; Abdoulaev, GS; Klose, AD; Lasker, J; Stewart, M; Netz, U; Beuthan, dan J: Near-infrared diffuse optical tomography. Disease markers, 18(5-6):313–337, 2002.

[HY16] Hoshi, Yoko; Yamada, Yukio: Overview of diffuse optical tomography and its clinical applications. Journal of biomedical optics, 21(9):091312–091312, 2016.

[Ib21] Ibtehaz, Nabil; Chowdhury, Muhammad EH; Khandakar, Amith; Kiranyaz, Serkan; Rahman, M Sohel; Tahir, Anas; Qiblawey, Yazan; Rahman, Tawsifur: EDITH: ECG biometrics aided by deep learning for reliable individual authentication. IEEE Transactions on Emerging Topics in Computational Intelligence, 6(4):928–940, 2021.

[Ji18] Jiang, Huabei: Diffuse optical tomography: principles and applications. CRC press, 2018.

[Kr20] Krivokuca, Vedrana; Gomez-Barrero, Marta; Marcel, Sébastien; Rathgeb, Christian; Busch, Christoph: Towards Measuring the Amount of Discriminatory Information in Finger Vein Biometric Characteristics Using a Relative Entropy Estimator. Handbook of Vascular Biometrics, p. 507, 2020.

[MHM20] McInnes, Leland; Healy, John; Melville, James: , UMAP: Uniform Manifold Approximation and Projection for Dimension Reduction, 2020.

[Qi18] Qiu, Xinwei; Kang, Wenxiong; Tian, Senping; Jia, Wei; Huang, Zhixing: Finger Vein Presentation Attack Detection Using Total Variation Decomposition. IEEE Transactions on Information Forensics and Security, 13(2):465–477, 2018.

[TY13] Tilton, Catherine J; Young, Matthew: Standards for Biometric Data Protection. In: Security and Privacy in Biometrics, pp. 297–310. Springer, 2013.

[USJ20] Uliyan, Diaa M; Sadeghi, Somayeh; Jalab, Hamid A: Anti-spoofing method for fingerprint recognition using patch based deep learning machine. Engineering Science and Technology, an International Journal, 23(2):264–273, 2020.

[Xi19] Xiang, Jinxi; Dong, Yonggui; Xue, Xiaohui; Xiong, Hao: Electronics of a Wearable ECG With Level Crossing Sampling and Human Body Communication. IEEE Transactions on Biomedical Circuits and Systems, 13(1):68–79, 2019.

[Yu05] Yu, Guoqiang; Durduran, Turgut; Lech, Gwen; Zhou, Chao; Chance, Britton; Mohler III, Emile R; Yodh, Arjun G: Time-dependent blood flow and oxygenation in human skeletal muscles measured with noninvasive near-infrared diffuse optical spectroscopies. Journal of biomedical optics, 10(2):024027–024027, 2005.